

This is the accepted manuscript made available via CHORUS. The article has been published as:

Systematic study of the hybrid plasmonic-photonic band structure underlying lasing action of diffractive plasmon particle lattices

A. Hinke Schokker, Floor van Riggelen, Yakir Hadad, Andrea Alù, and A. Femius Koenderink

Phys. Rev. B **95**, 085409 — Published 8 February 2017

DOI: [10.1103/PhysRevB.95.085409](https://doi.org/10.1103/PhysRevB.95.085409)

Systematic study of the hybrid plasmonic-photonic band structure underlying lasing action of diffractive plasmon particle lattices

A. Hinke Schokker,¹ Floor van Riggelen,¹ Yakir

Hadad,² Andrea Alù,^{2,1} and A. Femius Koenderink¹

¹*Center for Nanophotonics, FOM Institute AMOLF,*

Science Park 104, 1098 XG Amsterdam, The Netherlands

²*Department of Electrical and Computer Engineering, The University of Texas at Austin,*

1616 Guadalupe Street, UTA 7.215, Austin, TX 78712, USA

Abstract

We study lasing in distributed feedback lasers made from square lattices of silver particles in a dye-doped waveguide. We present a systematic analysis and experimental study of the band structure underlying the lasing process as a function of the detuning between the particle plasmon resonance and the lattice Bragg diffraction condition. To this end, as gain medium we use either a polymer doped with Rh6G only, or polymer doped with a pair of dyes (Rh6G and Rh700) that act as Förster energy transfer (FRET)-pair. This allows for gain respectively at 590 nm or 700 nm when pumped at 532 nm, compatible with the achievable size-tunability of silver particles embedded in the polymer. By polarization-resolved spectroscopic Fourier microscopy, we are able to observe the plasmonic/photonic band structure of the array, unravelling both the stop gap width, as well as the loss properties of the four involved bands at fixed lattice Bragg diffraction condition and as function of detuning of the plasmon resonance. To explain the measurements we derive an analytical model that sheds insights on the lasing process in plasmonic lattices, highlighting the interaction between two competing resonant processes, one localized at the particle level around the plasmon resonance, and one distributed across the lattice. Both are shown to contribute to the lasing threshold and the overall emission properties of the array.

Keywords: plasmonic antennas, lasing, distributed feedback, random lasers

I. INTRODUCTION

Organic distributed feedback lasers have been widely studied since the mid-nineties for their ability to provide large area lasing upon optical or electrical pumping, while being very simple to fabricate¹. Such lasers generally consist of an organic gain medium that is deposited as a thin layer over a periodically corrugated dielectric surface, with a periodicity chosen such that it offers an in-plane Bragg diffraction condition within the gain window^{2,3}. A wide range of emission wavelengths can be selected through the availability of a vast variety of organic fluorophores and fluorescent polymers, while the typically small corrugations over the surface can be realized through optical lithography, or soft imprint lithography^{4,5}.

More recently a different class of lasers was proposed that rely on plasmonic effects. Plasmonics uses the fact that free electrons in metals offer a collective resonance at optical frequencies⁶. This causes metal nanoparticles or nanostructured surfaces to provide highly enhanced and strongly localized electromagnetic fields upon irradiation, boosting the spontaneous emission rate of coupled fluorescent emitters⁷⁻⁹. When such plasmonic particles are placed in two-dimensional diffractive periodic arrays, they can also provide control over emission directivity and brightness, due to the hybridization of localized plasmonic resonances with grating anomalies associated with the array geometry and surrounding dielectric environment¹⁰⁻¹². In particular, these systems have been studied as substrates for Surface Enhanced Raman Scattering (SERS)¹³, sensing^{14,15} and solid-state lighting^{10,16}. Recently, several groups¹⁷⁻²⁰ have shown distributed feedback lasing in such plasmonic periodic systems. A significant difference with conventional distributed feedback lasers is that, while the dielectric perturbation is typically weak and non-resonant, for plasmonic systems the scattering strength per unit cell of the lattice can become very strong, and strongly dispersive, around the supported resonance. One practical advantage is that strong scattering implies broader stop gaps, which corresponds to smaller Bragg scattering lengths, or equivalently much smaller required device sizes for lasing, and large robustness to disorder²¹.

In earlier work²⁰, some of us presented the first experimental observation of the plasmonic band structure underlying lasing action of a plasmon particle lattice coupled to a dielectric waveguide that also provides gain. In this system Bragg resonance was established using diffraction by metal particles which are relatively strong scatterers compare to all-dielectric gratings. However, in that study the plasmonic particles were off resonance within the gain window and the lasing frequency set by the lattice periodicity. Therefore their individual scattering, while stronger than that of

dielectric corrugations, was still weak compared to the maximum attainable cross section. Likewise, in work by other groups^{17–19} on lasing in systems with surface lattice resonances (diffractive plasmonic resonances without assistance of a waveguide mode), the plasmon particle resonance frequency was not systematically varied. On the contrary, here we present a systematic study of the band structure underlying lasing when the plasmon resonance is tuned close to, and onto, the lasing condition. We identify a systematic dependence of the stop gap width on the scattering strength of the particles. Moreover, we find that, as the plasmon resonance crosses the lasing condition, the loss characteristics of the supported bands interchange and, as a consequence, also the stop gap edge at which lasing occurs moves from the low to the high end of the gap. These findings are in full agreement with an electrodynamic point dipole analytical model that we develop in this work, accounting for near- as well as far-field interactions among the particles mediated by the waveguide structure in which they are deposited. This paper is structured as follows. In section II, and III, we develop and analyze a rigorous theoretical study of the structure’s complex-valued dispersion relation based on this dipolar model. In section IV and V we introduce our experimental methods and report on the spectroscopy of our gain medium. In section VI,VII we analyze band structure measurements, showing that they validate our theory for the competing resonant phenomena behind the lasing effect. We close by a real-space full-wave analysis in section IX.

II. SEMI-ANALYTICAL MODEL

In this section we theoretically analyze the mode structure of two-dimensional plasmon particle lattices embedded in planar waveguides using the discrete dipole approximation. The geometry of interest is an infinite square lattice of silver cylindrical particles with periodicity d embedded in a high index slab that acts as waveguide and through doping also acts as gain medium (Figure 1(a)). Commensurate with the experiments reported here and in Ref. 20, we take this slab to have a thickness $h = 450$ nm and relative dielectric constant $\epsilon_2 = 2.79$ (equivalent to the polymer SU8). The slab is surrounded by air on one side ($\epsilon_1 = 1$, located at $z > h$), and glass on the other (substrate with $\epsilon_3 = 2.25$ located at $z < 0$). The array is embedded close to the SU8-glass interface, as shown in Fig.1. The air/SU8/glass stack supports a single transverse electric (TE) and a single transverse magnetic (TM) mode of almost identical mode index (1.55, calculated using the method of Urbach and Rikken²²). Mode profiles (Fig. 1(c,d)) evidence that the TE mode has a strong polarization component in the plane in which the particles are polarizable, while the TM mode has only

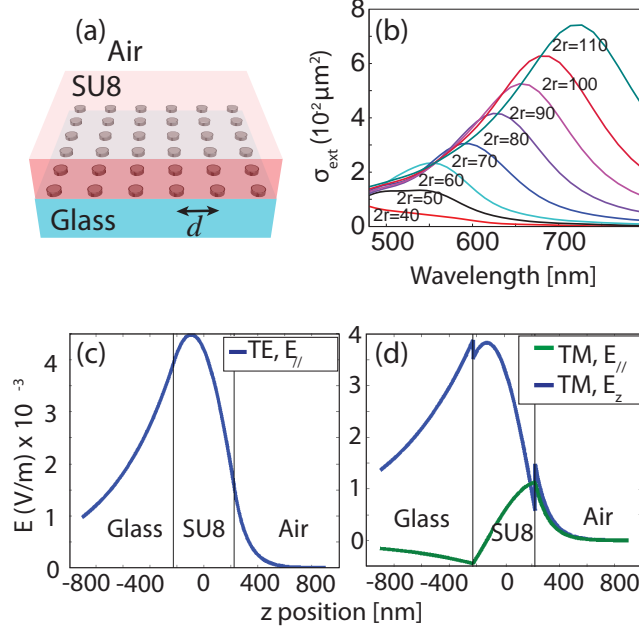


FIG. 1. (a) Schematic of the sample geometry, consisting of a periodic square lattice of thin silver discs (pitch d) on a glass substrate, embedded in a high index polymer SU8 that supports a waveguide mode and is doped with organic dye to provide gain. (b) Extinction cross section according to FDTD simulations (Lumerical using CRC tabulated optical constants) of single silver disks of various radii r embedded in the air/SU8/glass system, under normal incidence from the glass side. (c,d) Electric field profile of the single TE and single TM mode supported by the structure. In (c) the in-plane field is perpendicular to the in-plane wave vector, while in (d) it is along it.

71 weak overlap. To understand the physics of the particles' interaction with the modes, we have con-
72 ducted FDTD simulations (Lumerical, using tabulated optical constants²³) to determine extinction
73 cross sections of single particles in the stratified system (incidence from the glass side). As the
74 particle diameter, $D=2r$, increases, the extinction crosssection (Fig. 1(b)) strongly increases, and
75 furthermore exhibits the well-known shift to longer wavelengths due to dynamic depolarization
76 effects^{24–26}. For $D > 60$ nm, the dipolar resonance has a distinct Lorentzian shape, and is well
77 separated from the features at wavelengths $\lambda < 500$ nm, that are due to intraband features in the
78 dielectric constant.

79 Our goal is to calculate the passive array dispersion of the composite system including loss, as
80 well as the relation between the local surface plasmon resonance excitation strength of the array
81 and the efficiency of coupling to far-field radiation. Since Ohmic and radiation loss are impor-
82 tant we target a complex-valued dispersion relation, where the imaginary part of wavenumber

quantifies loss. Lasing is established by a combination of feedback and amplification processes. Particularly, in distributed feedback lasers the former is achieved by a distributed backward Bragg resonance, a result of coupling between counter-propagating slab modes¹. The threshold for lasing is determined by the quality factor of the feedback mechanism in the absence of gain. Therefore, dominant lasing will take place in the frequency range for which the quality factor of the feedback mechanism is the highest, namely the frequency regions where the imaginary part of the complex dispersion wavenumber of the resulting coupled slab modes, in the absence of gain, is minimal. At the same time, to observe lasing the emission must be able to couple out into the far field. Our aim is hence to isolate the low-loss points of the complex-valued dispersion diagram that at the same time are not forbidden from coupling to radiation. Since this type of passive-system model accounts for linear loss, but not gain dynamics or spontaneous emission noise, it only gives insight up to threshold, answering what modes will lase first, but not what their nonlinear physics will be well above threshold.

In order to rigorously tackle the above threshold dynamics, one may apply a time-domain approach, such as the Finite Difference Time Domain method, which can be used to calculate the real-space field distribution, which is mutually and nonlinearly affected by the 4-level system describing the medium through a simultaneous solution of the time-dependent Maxwell equations and the active medium rate equations²⁷. Unfortunately, such an approach is limited to finite structures and thereby cannot provide the complex k -vector details that naturally emerge in our linear k -vector analysis. Full wave solution methods with periodic boundary conditions naturally deal with infinite systems. However the Bloch-Floquet boundary condition imposes the wave vector, as opposed to the physics of a lasing process that selects the wave vector. With such real-space methods one can in principle sample k -space to map out dispersion and loss, by doing many simulations that sample k -space point by point. This approach is limited to real wave vectors and requires significant computational effort. An alternative approach is proposed in²⁸, where the discrete dipole method is used in the frequency domain, but with the Green's function of an infinitely homogeneous medium (therefore no slab modes are considered). In order to obtain a time-domain model that includes the 4-level system dynamics, the periodic system response, i.e., the dipole lattice sum, is approximated using the assumptions that (a) the lattice response at diffraction resonance is a Lorentzian single resonance, and (b) that lasing occurs at $k=0$. Hence, although this analysis captures interesting features of the lasing process above threshold, it does not treat the lasing as a process that originates from noise and settles at the minimal loss $k(\omega)$ points. Using our linear

115 model we find, in accord with our measured data, that not only that lasing takes place at $k \neq 0$ but
 116 also that under certain conditions, that are discussed below, there are two rather than one lasing
 117 points $k(\omega)$. In this case, the frequency response becomes close to the diffraction resonance with
 118 the profile of two overlapped Lorentzians. Therefore we believe that to gain a complete picture of
 119 the lasing process in such a plasmonic array system various perspectives are required, as proposed
 120 in^{27,28} and²⁹ for the above threshold behaviour as well as the linear k-space model discussed in
 121 this paper, below threshold, that fully accounts for the loss mechanism and hence for the lasing
 122 initiation dynamics, as a battle between gain and loss.

123 As method of choice for our work we focus on a semi-analytical model that describes the
 124 particles as strong dipolar scatterers, and accounts for all the electrodynamic multiple scattering
 125 interactions in the lattice that may take place via the waveguide. Such electrodynamic point dipole
 126 models for lattices have been considered in earlier work mainly in the context of lattices in a
 127 homogeneous background^{30–33}, with a few exceptions that consider also the presence of a dielec-
 128 tric slab^{34,35}. It is important to distinguish this method from coupled mode theory typically used
 129 for conventional periodically corrugated dielectric waveguides³⁶. In solid-state terms, such plane
 130 wave expansion methods are equivalent to a “nearly-free photon” approach, where the waveguide
 131 dispersion relation folds at the edges of the Brillouin zone, and where the small index contrast
 132 causes minute stop gaps to open up. This type of model is not applicable for the case at hand,
 133 since the plasmonic particles are characterized by strong individual scattering, which does not
 134 perturb, but instead significantly modifies the band structure. This is also evident in numerical
 135 plane wave expansion approaches to periodic plasmon particle systems that either do not converge
 136 or need of order 10^3 plane waves to resolve the plasmon particle resonance despite the fact that at
 137 the operation point (2nd order Bragg diffraction) only 4 diffraction orders couple. Since the plas-
 138 monic particles are designed to operate around their dominant dipolar resonance, we have a strong
 139 basis to assume that the particle’s interaction is essentially dipolar. For this reason, our analytical
 140 approach employs an electrodynamic dipole model with Ewald summation to deal with all the
 141 retarded dipole-dipole interactions mediated by the waveguide slab. This model builds on recent
 142 implementations of periodic point-dipole lattice models that successfully describe the hybridiza-
 143 tion of localized plasmons with propagating and evanescent photonic diffraction orders^{31–33,37–42}.

144 The dipolar response of a scatterer is described by its polarizability response $\alpha(\omega)$, which for a

145 resonant scatterer in the quasistatic limit reads³²

$$\alpha_{\text{static}}(\omega) = \frac{V\omega_0^2}{\omega^2 - \omega_0^2 - i\omega\gamma} \quad (1)$$

146 (in CGS units, with ω angular frequency, ω_0 the particle resonance, γ an Ohmic damping rate, and
 147 V an (effective) particle volume), in the limit in which the response is locally approximated by
 148 a single resonance⁴³. One must include radiation damping^{30,32} to turn this polarizability into its
 149 dynamic form, which is required to build a self-consistent electrodynamic theory with a correct
 150 energy balance. For a particle in free-space, the dynamic polarizability reads

$$\frac{1}{\alpha} = \frac{1}{\alpha_{\text{static}}} - i\frac{2}{3}k^3 \quad (2)$$

151 (with $k = n\omega/c$). However, our case is somewhat different, since the particles are located inside
 152 a dielectric layered system which affects both the radiation damping correction, as well as red
 153 shifts the resonance frequency. In the following, we use the model given in Eq. (1) and Eq.
 154 (2), and fit the plasmonic resonance model to our full wave simulations of a single inclusion in
 155 the dielectric stratified system (discussed further below). This fit yields a resonance frequency
 156 $\lambda_0 = 334 \times 10^{-9} + 3.6 \times 2r[m]$ and a damping rate $\gamma = 0.05\omega_0$ where $\omega_0 = 2\pi c/\lambda_0$, $k =$
 157 $2\pi\sqrt{\epsilon_2}/\lambda_0$. It turns out that, while in rigorous terms the radiation damping in Eq. (2) should be
 158 corrected using the imaginary part of the Green's function at the location of the particle³⁴, it is
 159 a fair approximation to simply use Eq. (2) since the Ohmic damping in the particles dominates
 160 compared with the radiation loss, and its modification is also partially being taken into account by
 161 the fitting. Using this model, we can use a fitted analytical expression for the polarizability of the
 162 particles, which yields a very good approximation to the scattering cross section we obtain from
 163 full wave simulations in the diameter range 40 – 110 nm. As particles used in experiments are
 164 flat in the z -direction (30 nm height, versus 100 nm diameter typically), we constrain the particle
 165 polarizability to the xy -plane, meaning that dipole moments can only be excited in plane.

The array is periodic by translation over d in both the x and y directions, and thereby we can
 assume that the induced dipole moments assume a Bloch form $\mathbf{p}_{mn} = \mathbf{p}_{00}e^{id(nk_x + mk_y)}$, where
 m, n are the particle indices and (k_x, k_y) is the wavevector of the excited collective plasmonic
 mode parallel to the layers. For a lattice driven by an incident field of the form $\mathbf{E}_{in}e^{id(nk_x + mk_y)}$,
 the induced dipole moments are given by

$$\mathbf{p}_{00} = \alpha \left[\mathbf{E}_{in} + \sum_{n,m \neq 0,0} \mathbf{G}(\mathbf{r}_{00}, \mathbf{r}_{mn}) \mathbf{p}_{mn} \right]$$

or equivalently $\mathbf{p}_{00} = \frac{1}{\alpha^{-1} - \mathbf{C}} \mathbf{E}_{in}$ with

$$\mathbf{C} = \sum_{n,m \neq 0,0} \mathbf{G}(\mathbf{r}_{00}, \mathbf{r}_{mn}) e^{id(nk_x + mk_y)}.$$

Here the term \mathbf{C} accounts for all dipole-dipole interactions and is also known as lattice sum^{31–33,37–42}. The dyadic Green function \mathbf{G} accounts for the full physics of the stratified system, meaning that it includes the TE and TM guided mode that the assumed slab supports, plus the continuous spectrum that accounts for radiation into the substrate and superstrate.

From this starting point, we can make several simplifications. The 2nd order Bragg resonance on which lasing occurs at the Γ -point $(k_x, k_y) = (0, 0)$ takes place in the two orthogonal directions parallel to the lattice primitive vectors (diffraction by lattice vectors $2\pi/d(\pm 1, 0)$ and $2\pi/d(0, \pm 1)$). Given the symmetry, without loss of generality we can analyze the $k_x = 0$ slice of the dispersion relation (propagation direction is \hat{y}), in which case the dipole polarization is along \hat{x} . Hence, the modal matrix problem reduces to the simplified scalar equation

$$\Delta(\omega, k_x, k_y) \equiv \alpha(\omega)^{-1} - C(\omega, k_x, k_y) = 0. \quad (3a)$$

176

$$C(\omega, k_x, k_y) = \sum' G_{xx}(\omega, \mathbf{r}_{00}, \mathbf{r}_{mn}) e^{id(mk_x + nk_y)}. \quad (3b)$$

In Eq. (3b), the symbol \sum' denotes summation over all indices except $(m, n) = (0, 0)$, and G_{xx} is the xx component (the \hat{x} component of the electric field due to a \hat{x} polarized dipole) of the electric Green's function tensor in the 3-layer dielectric medium host.

Taking the full spectral content of the Green's function into account in the infinite summation in Eq. (3b) is numerically challenging, as the Green function in a stratified medium is generally expressed in angular spectrum representation as a parallel wave vector integral that includes guided modes as poles on top of a radiation continuum. We expect the Green function to be dominated by its poles on basis of physical considerations: First, the distance between the particles corresponds to Bragg resonance at the TE mode, and second the particles strongly overlap with the TE waveguide mode as consequence of their position in the slab, and their anisotropic, flat, geometry. Since the TE and TM modes of the slab (in absence of particles) are very close in dispersion, we expect significant TE-TM coupling. On this basis, we employ the assumption that we can neglect any continuous spectrum contribution to the Green's function, yet need to retain the TE and TM guided mode contribution to the Green function. Based on these considerations, we replace the full Green's function G_{xx} with its modal part, G_{xx}^m including both TE and TM mode contributions,

192 i.e. $G_{xx}^m = G_{xx}^{TE} + G_{xx}^{TM}$, where the TE and TM contributions are separately given by

$$G_{xx}^{TE} = 2A_{TE} \left[H_0^{(1)}(k_{TE}\rho) + \frac{\partial_{x'}^2 H_0^{(1)}(k_{TE}\rho)}{(k_{TE})^2} \right] \quad (4a)$$

193

$$G_{xx}^{TM} = -2A_{TM} \left[\frac{\partial_{x'}^2 H_0^{(1)}(k_{TM}\rho)}{k_{TM}^2} \right] \quad (4b)$$

194 where $\rho = \sqrt{(x - x')^2 + (y - y')^2}$, k_{TE}, k_{TM} are the wavenumbers in the transverse direction of
 195 the guided slab mode in the absence of the array, given by a solution of the corresponding mode
 196 transcendental equation²². The amplitudes A_{TE}, A_{TM} are given by

$$A_X = \frac{k_0^3}{4\pi\epsilon_0} \frac{i}{2\eta_0} 2\pi\xi_X g(z, z, \xi_X), \quad X = TE, TM \quad (5)$$

197 where $\xi_X = k_X/k_0$, and g is the 1D Green's function given in Appendix A. The infinite summation
 198 in Eq. (3) is slowly converging due to the inverse square root dependence of the Hankel function
 199 with respect to its argument. However, the convergence can be significantly accelerated applying
 200 the Ewald summation technique, adapted to the problem at hand (Appendix B).

201 Solution of Eq. (3) provides the complex-valued dispersion of the collective plasmonic ex-
 202 citation of the array in absence of gain. The lasing process in the structure is expected to build
 203 up in the regions of the frequency - wavenumber plane where the imaginary part of the complex
 204 wavenumber is minimal. To observe lasing, radiation must also couple out of the waveguide. Fo-
 205 cusing on x-polarized excitation, the dipolar moment p_{00} due to an impinging x-polarized plane
 206 wave with amplitude E_0 at ω with $(0, k_y)$ is given by $p_{00} = E_0/\Delta(\omega, 0, k_y)$. By reciprocity, the
 207 radiated field due to a dipole strength p_{00} at ω and (real) $(0, k_y)$ can be calculated from the reverse
 208 problem, i.e., from the induced dipole strength p_{00} induced by an incident plane wave of given
 209 strength E_0 , incident at ω with $(0, k_y)$. Therefore, the quantity $1/\Delta(\omega, 0, k_y)$, essentially indicates
 210 the coupling between x-polarized induced dipoles and x-polarized far-field radiation with $k_{||} = k_y$.
 211 In the following section, based on this analytical model, we explore how the interplay of these two
 212 resonances controls the lasing mechanism in the lattice.

213 III. THEORETICAL PREDICTION OF THE LASING CONDITIONS

214 Fig. 2 shows the coupling efficiency between the excited dipolar moments and far-field radia-
 215 tion in a relatively wide frequency region around the TE Bragg resonance frequencies as grayscale
 216 where, black (white) represents poor (strong) radiation. Panels (b)-(d) correspond to three distinct

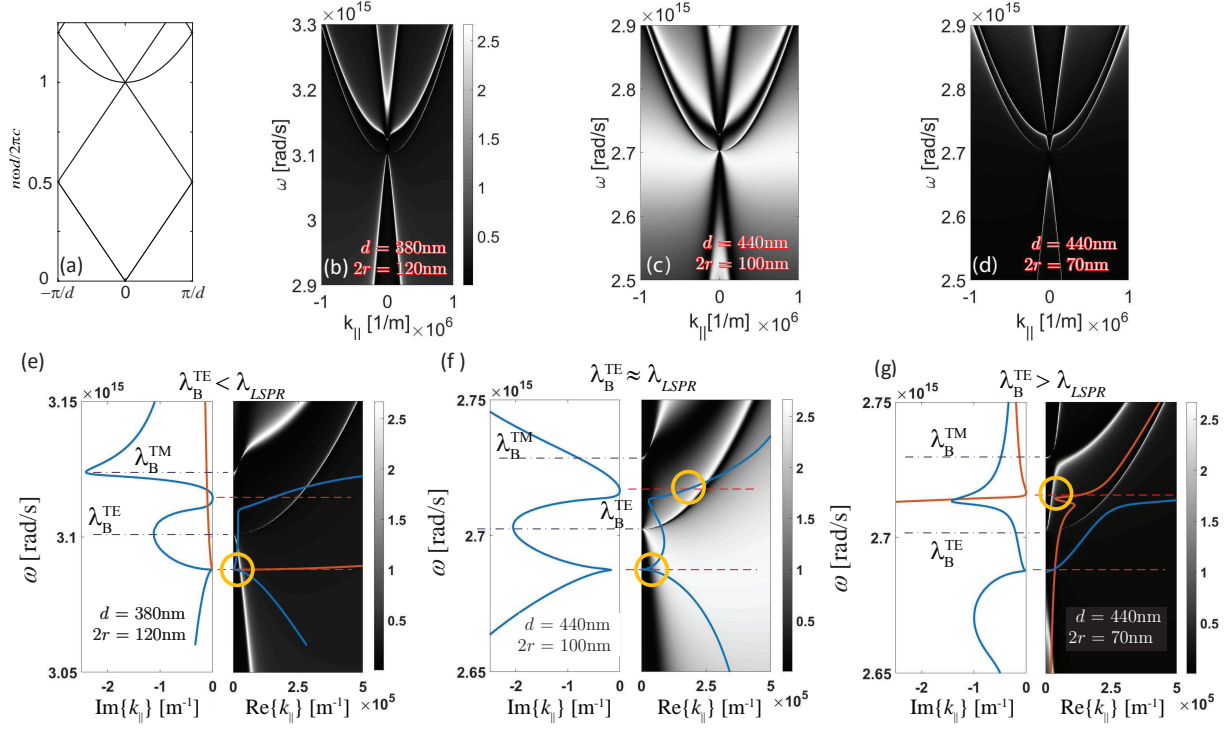


FIG. 2. (a) Sketch of the free photon approximation to the dispersion relation between k_y on the x -axis, and dimensionless frequency $n\omega d/2\pi c$, where d is the lattice pitch and n the mode index. The dispersion relation folds back by diffraction at $2\pi/d(0, \pm 1)$ resp. $2\pi/d(\pm 1, 0)$ to give the lines resp. parabolas crossing at $k_y = 0$ (2nd order Bragg diffraction). (b-d) coupling efficiency between x -polarized dipolar excitation and x -polarized far-field for incidence in the k_x zero plane (varying real ω and k_y). (a) $\lambda_B^{TE} < \lambda_{LSPR}$, (b) $\lambda_B^{TE} \approx \lambda_{LSPR}$, (c) $\lambda_B^{TE} > \lambda_{LSPR}$. Panels (e-g): the left panels show the dispersion of the imaginary part of k_y , while curves in the righthand panels show the corresponding real part of the dispersion relation (blue and brown curve indicating different dispersion branches). The background grayscale shows the efficiency of coupling taken from panels (b-e). We expect that lasing is observed at a minimum of $\text{Im}k_y$ (indicated by red dashed lines) and simultaneously good outcoupling (conditions marked by circles). For reference in the left panels we indicate with black dashed lines the free-photon Bragg conditions for the TE and TM waveguide mode. Panels (e-g) are for the same parameters as (b-d), meaning that they correspond to $\lambda_B^{TE} < \lambda_{LSPR}$, resp. $\lambda_B^{TE} \approx \lambda_{LSPR}$ and $\lambda_B^{TE} > \lambda_{LSPR}$.

cases of interest, $\lambda_B^{TE} < \lambda_{LSPR}$, $\lambda_B^{TE} \approx \lambda_{LSPR}$, and $\lambda_B^{TE} > \lambda_{LSPR}$, respectively, where λ_{LSPR} is the wavelength of the plasmonic particle resonance frequency, and λ_B^{TE} is the free-space wavelength at which the 2nd order TE mode Bragg resonance takes place. The salient feature is an

anticrossing at $k_x = k_y = 0$ and ω around $3.1 \cdot 10^{15} \text{ s}^{-1}$ that involves four bands. These originate from the folded free-photon dispersion (Panel (a)), that generates two linear bands (dispersion $k_y = n_{TE}\omega/c$ diffracted by $2\pi/d(0, \pm 1)$), and two parabolas (diffracted by $2\pi/d(\pm 1, 0)$). While in the case of significant red and blue detuning from the plasmon resonance (tuned by particle size) the photon dispersion is recognizable in the coupling efficiency $1/\Delta$ as narrow features close to the free photon dispersion, for the on-resonance case, the dispersion is qualitatively different. In Figure 2(e-g) we zoom in at the frequency of the TE Bragg condition and plot the coupling efficiency (grayscale map) together with the complex dispersion of the collective plasmonic excitation, obtained as a solution of Eq. (3). This figure allows to predict at which frequencies lasing is expected.

The curves (blue only or blue and brown) in each panel represent the relevant parts of the complex dispersion. In the left (right) side of each panel, we show the dispersion of the imaginary (real) part of $k_{||}$. Additional dispersion branches with much higher imaginary part are not shown, since we focus only on branches with an imaginary part close to zero that can contribute to lasing. For all three detuning scenarios considered, there are two frequencies for which the imaginary part of $k_{||}$ has a minimum. If only a single waveguide mode would contribute (e.g., TE-only), only a single minimum would be expected, as one would expect one of the two stop gap edges to correspond to strong overlap (large loss), and one with weak overlap (low loss), of the corresponding Bloch mode with the particles. The fact that two minima occur is hence a sign of TE-TM coupling. While each minimum indicates a distributed resonance for which field amplification is expected when gain is added, observing clear laser output also requires efficient outcoupling. In other words, we now focus on simultaneously finding a frequency corresponding to minimum of $\text{Im}\{k_{||}\}$, and at the same time significant outcoupling as indicated by the grayscale colormaps on the right hand side of each panel in Fig. 2(e-g) (for $\text{Re}\{k_{||}\}$ near zero).

In the first scenario, shown in Fig. 2(e), $\lambda_B^{TE} < \lambda_{LSPR}$ the only point for which we have simultaneously low imaginary part of $k_{||}$ and significant coupling efficiency is at a frequency just above the kinematic TE Bragg condition (dashed line). In the opposite-detuning case, Fig. 2(g), $\lambda_B^{TE} > \lambda_{LSPR}$, the only point with low imaginary part of $k_{||}$ and simultaneously good outcoupling is below the kinematic TE Bragg condition. Finally, in the case in which particle resonance and lasing condition are tuned close to each other (Fig. 2(f), $\lambda_B^{TE} = \lambda_{LSPR}$), there are two points, one above and one below the TE Bragg condition, where this condition is satisfied. These results hence predict that for plasmon resonance and Bragg condition detuned from each other, one expects a

252 distinct splitting in the dispersion relation, with lasing occurring always on the stop gap edge that
 253 is closes to the plasmon resonance. For the intermediate case, both stop gap edges would lase. We
 254 further note that the proximity of the imaginary part of $k_{||}$ to the zero axis, and the brightness of
 255 the greyscale images representing coupling strength to radiation are expected to relate to the lasing
 256 mode loss (and hence, required threshold) and lasing outcoupling efficiency. In the following,
 257 we discuss a campaign of experiments analyzing plasmonic arrays satisfying the three detuning
 258 conditions outlined in Fig. 2. Sections IV,V report on methods, while measured band structure
 259 results as function of the detuning between Bragg condition and plasmon resonance are discussed
 260 in section VI and compared to the point dipole model in section VII.

261 **IV. SAMPLE GEOMETRY, SET UP AND CHARACTERIZATION OF THE GAIN MEDIUM.**

262 We fabricated silver particle arrays using electron beam lithography on ZEP resist, thermal
 263 evaporation of silver, and lift-off, on standard glass coverslips (Menzel, borosilicate). The square
 264 lattices are embedded in SU8. We study cylindrical particles with varying diameter (about 60 to
 265 120 nm), and a height of about 30 nm. Since previously we established²⁰ that only silver gives
 266 advantageous results for plasmon lasers, owing to the much higher loss in other metals, this study
 267 focuses on silver. The dye-doped SU8 film of about 450 nm thickness is prepared by spincoating
 268 from a solution that is prepared by mixing equal parts of SU8-2005 (SU8 in cyclopentanone, 45%
 269 solids, Microchem) and cyclopentanone in which the dye is mixed. As gain medium we have used
 270 two systems. On one hand, with Rh6G as dye (5 mM in cyclopentanone), we can achieve gain
 271 near 590 nm. This requires small pitches, between 360 and 400 nm, and gives access to cases with
 272 particles red-detuned from the gain medium. With a gain medium at 700 nm, and concomitantly
 273 larger lattice pitch of 460 nm we can access blue detunings. To obtain a gain medium in this range
 274 that we can actually pump with our pump laser at 532 nm, we use a pair of dyes, namely 5 mM of
 275 Rh6G that absorbs the pump light, and acts as donor for Förster energy transfer to Rh700 which
 276 provides the gain, and which we have included at 0, 0.5, 3, 5 and 10 mM concentration. If one
 277 assumes that after spincoating all material except the cyclopentanone remains, dye concentrations
 278 in the film are approximately 2.2 times the nominal dye concentrations in solution. By ellipsometry
 279 we verified that the dye doped films have a refractive index of around 1.60, resulting in a single TE
 280 and a single TM mode that both have an effective index of about 1.55. We note that as the particle
 281 diameter is changed to control detuning, this changes the scattering strength at the lasing condition

282 *both* because there is simply more polarizable matter per particle *and* because the resonance shifts.

283 We collect fluorescence emission that is resolved in frequency and parallel wave-vector using
 284 the set up presented in Ref. 20 in which the sample is placed on an inverted optical microscope
 285 equipped with a 100× Nikon objective (Plan Apo NA=1.45). We excited a 40 μm spot using 532
 286 nm light offered in a 0.5 ns pulse with energy per pulse controlled in the range 0-20 nJ via an
 287 acousto-optical modulator. We also performed spectroscopy and fluorescence lifetime measure-
 288 ments on dye-doped films without plasmon particles to calibrate the dye system. To this end we
 289 used the fluorescence lifetime and spectroscopy set up presented in Ref. 44.

290 V. SPECTROSCOPY OF CONSTITUENTS & FRET

Figure 3 shows reference results for the gain medium composed of the FRET pair Rh6G and Rh700. Using samples without plasmonic particles, and low excitation amplitude, we measured emission spectra at fixed Rh6G concentration, and various Rh700 concentrations. Emission at the short wavelength end is clipped by a 540 nm longpass filter. Evidently the strong Rh6G emission band (550 to 620 nm) rapidly decreases in intensity as Rh700 is mixed into the film, while at the same time strong emission of the Rh700 dye (650 to 750 nm band) arises. At a one-to-one ratio (where the nominal dye concentrations prior to mixing with SU8 is 5 mM) the Rh6G emission has almost completely vanished. For larger concentration of Rh700, the Rh700 emission decreases, and redshifts. The disappearance of Rh6G emission and the appearance of Rh700 fluorescence, that is poorly pumped by 532 nm directly, is commensurate with Förster Resonance Energy Transfer” (FRET). As usual⁴⁵ we define the energy transfer efficiency as $E = 1 - F_{DA}/F_D$ where F_D is the integrated (detector-corrected) spectral intensity of the donor-only sample, while F_{DA} is the integrated spectral intensity of the acceptor. Figure 3(c) shows the energy transfer efficiency deduced from the data in (b) as a function of the nominal concentration (symbols) alongside the prediction⁴⁵⁻⁴⁷

$$E = -\sqrt{\pi}\gamma e^{\gamma^2}(1 - \text{erf}\gamma)$$

that is appropriate for FRET in 3D homogeneous media. This expression depends only the dimensionless concentration C/C_0 via the parameter

$$\gamma = \frac{\Gamma(1/2)}{2} \frac{C}{C_0} \quad \text{with} \quad C_0 = \left(\frac{4}{\pi} R_0^3 \right)^{-1},$$

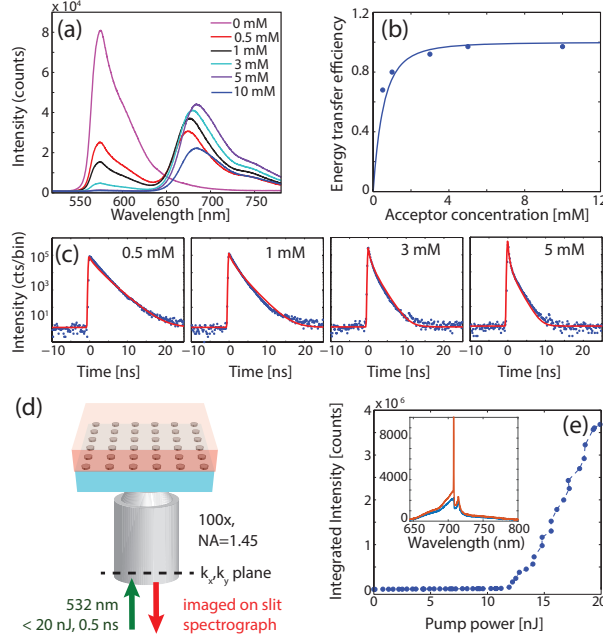


FIG. 3. (a) Emission spectra of dye mixtures under weak pumping. Here the concentration of Rh6G is fixed to 5 mM and the concentrations given in the figure represent Rh700 concentrations. (b) FRET efficiency curve from spectral integrals. The horizontal axis represents the concentration of Rh700, and the vertical axis represents energy transfer efficiency from the donor to the acceptor. (c) Lifetime traces for four concentrations (0.5, 1, 3 and 5 mM) of Rh700. The solid curves plotted through the data points are FRET theory where no adjustable parameter is used except a vertical scaling. (d) Sketch of the lasing set up consisting of a inverted fluorescence microscope used in back focal plane spectral imaging mode. (e) Spectra (inset) at pump powers just below (10 nJ blue curve) and just above (15 nJ, orange curve), considering only a narrow band of wavevectors around $k_y = 0$. Note the stop gap, and lasing on the blue edge of the stop gap. The intensity of the lasing peak shows distinct threshold behavior.

where Γ represents the Gamma-function. We obtain a reasonable fit to the data for a critical concentration $C_0 = 0.9$ mM. Correcting for the difference between nominal concentrations *before* spincoating this result implies $C_0 = 2.2 \times 0.9$ mM in the SU8, which in turn translates to a Förster radius of about $R_0 = 5.5$ nm. Since this is on par with expected Förster radii⁴⁵, we conclude that the concentration dependence of spectra is consistent with FRET.

As independent check, we also measured fluorescence decay traces of the donor emission. If energy transfer is due to FRET, decays should be given by⁴⁶

$$I_D(t) = I_0 \exp \left[-t/\tau_D - 2\gamma(t/\tau_D)^{1/2} \right] \quad (6)$$

where τ_D is the donor decay time. Figure 3(d) shows measured decay traces at various concentrations alongside the prediction Eq. 6 convoluted with the instrument response function of our setup. We note that for this comparison we only adjust the overall scaling I_0 , but adjust neither $\tau_D = 3.4$ ns which is taken from a donor-only measurement, nor γ , which is taken from the spectral data. We note excellent correspondence, especially given that no parameter except overall scaling was adjusted. We identify the one-to-one 5 mM sample as most suited for our gain measurements as it provides strong Rh700 emission by FRET from Rh6G pumped by our 532 nm pump laser. From here onwards, in this paper we focus on samples with this gain medium, referring to them simply as "Rh700 samples".

It should be noted that in this paper we will not deeply discuss any *above*-threshold data, instead focusing on answering which mode reaches threshold (first) depending on the detuning between plasmon and Bragg condition. In order to show that lasing does occur (for all the samples we report on), Fig. 3 shows an exemplary result for a sample with particle size $2r = 74$ nm in diameter and pitch of 460 nm, lasing at 710 nm, using the Rh6G:Rh700 dye mixture as gain medium. The spectra are obtained using the inverted fluorescence microscope in Fourier imaging mode (Fig. 3(d)). At pump powers below about 12 nJ, the spectrum (panel (e), obtained by integrating only a narrow band of emission directions around $k_y = 0$) is similar to that on substrates with no particles, except for the appearance of a shallow gap near 715 nm. At the blue edge of this gap a narrow lasing peak appears for pump powers above 12 nJ. Tracing the intensity in a 5 nm wide spectral bin around the narrow lasing peak shows clear threshold behavior²⁰.

VI. BAND DIAGRAMS

Figure 4 shows measured ω, k diagrams of fluorescence below threshold. The measurements generically display two linear bands, as well as the expected parabolic feature, with a distinct anti-crossing centered around $2.63 \cdot 10^{15} \text{ s}^{-1}$ (715 nm, in accord with $1.55d$). The most notable feature in Fig. 4 that is distinct from the free photon folded dispersion relation sketched in Figure 2(a) is that the two parabolic bands are not degenerate but distinctly split. Such a splitting is also observable in the calculated dispersion for the point dipole model. In particular, Fig. 2(d,g) corresponds to a particle size/pitch combination that can be compared with the data in Fig. 4(d), where the reader is admonished that the data extends over a wider frequency- and wavenumber scale. In addition, the linear bands also show a stop gap, with band edges coincident with the minima of the parabola.

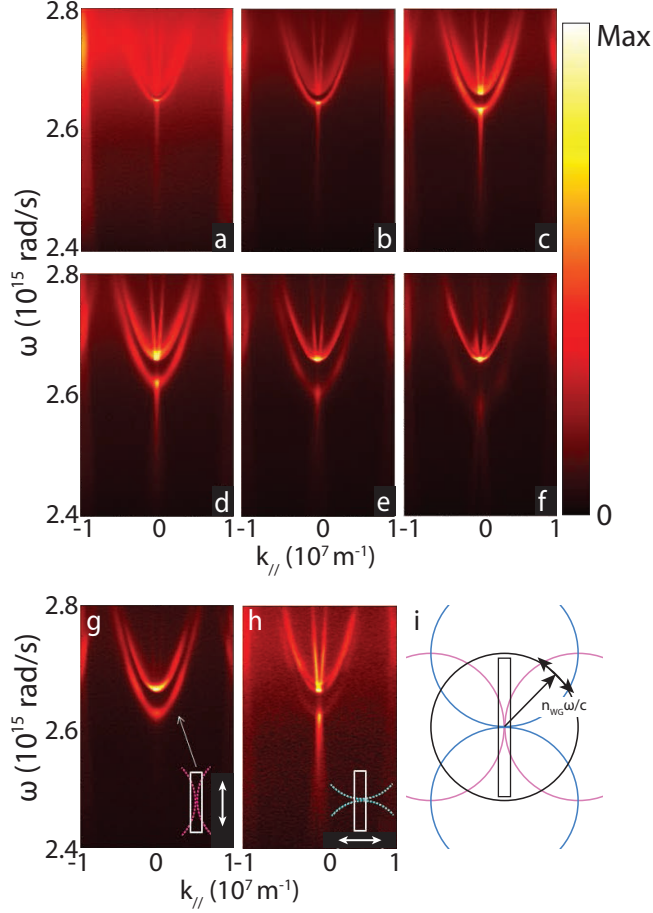


FIG. 4. Fluorescence (pumping below threshold) mapped in $\omega - k$ space as function of plasmon particle diameter, where the diameter varies from 53, 61, 74, 82, 86 to 95 ± 5 nm for panels (a-f), for samples with pitch $d = 460$ nm, using the Rh6G:Rh700 dye mixture, taken below threshold. Maxima are 5350, 8600, 11650, 14300, 25200, and 27950 counts/ $\mu\text{J}/\text{shot}$, respectively. Note how the stop gap increase in size. Panels (g,h): Polarization-resolved dispersion measurements for particle diameter of 86 nm, taking polarization along and perpendicular to the spectrometer slit. Panel (i): sketch of parallel momentum space. At a fixed frequency ω (here chosen at 2nd order Bragg diffraction), the slab waveguide mode appear as a circle of radius $n_{WG}\omega/c$ centered at the origin (black), and due to diffraction by the lattice repeated every reciprocal lattice vector $2\pi/d(m, n)$ (color coded). For the TE waveguide mode, the electric field polarization is in-plane, normal to the momentum. The slit (rectangle) maps a slice of momentum space. In (g) and (h) the color bar maximum is at 5500 resp 2400 counts per μJ of pump power.

328 This stop gap corresponds to the narrow gap visible also in Fig. 3(e,inset) around 715 nm, at the
 329 blue edge of which lasing occurs once threshold is exceeded.

330 Fluorescence in momentum space is expected to show distinct structure tracing out features
 331 close to the waveguide-array dispersion^{10,20}, commensurate with the predictions that the outcou-
 332 pling efficiency of the excited lattice will depend on frequency and angle (see maps of $1/\Delta(\omega, k_y)$
 333 in Fig. 2(b-d)). Figure 4(a-f) shows the progression of the measured band structure as we increase
 334 particle size. Clearly, the band structure stays qualitatively identical up to a particle size of 86 nm
 335 diameter, however, with a distinct increase in stop gap width. For particles above 95 nm in di-
 336 ameter, the band structure develops a qualitatively different appearance, both in terms of avoided
 337 crossing geometry, and in terms of the widths of the various bands. This is the regime where
 338 particles and lasing condition come in resonance, whereas for smaller diameters, the particles are
 339 blue-shifted with respect to the Bragg condition that is set by the lattice.

340 The polymer slab supports two modes, the fundamental TE and fundamental TM mode, as
 341 reported in Fig. 1(c,d). According to our modeling both participate in setting the geometry of
 342 the anticrossing in Fig. 2, although outcoupling is predominantly through the TE waveguide. To
 343 verify this assertion we collected data on a series of samples using a linear polarizer in front of
 344 the spectrometer slit. To understand the measurement, we refer to a sketch of the repeated zone
 345 scheme dispersion that is projected on the spectrometer entrance plane (Fig. 4i). Fluorescence
 346 is expected to dominantly be emitted into the waveguide mode. Since back focal plane imaging
 347 directly maps $k_{||}/k_0$, this would appear on our detector as a ring that is $n_{\text{TE,TM}} \approx 1.55$ times
 348 bigger than the free space light cone, if it weren't for the fact that the objective clips the signal to its
 349 NA of 1.45. Bragg diffraction causes the dispersion to be replicated every reciprocal lattice vector
 350 $\mathbf{G} = 2\pi/d(m, n)$ (with m, n integer), leading to a set of intersecting circles of radius $1.55k_0$ on the
 351 spectrometer entrance port²⁰. In our measurement we only collect a slice along one axis (labelled
 352 k_y), spectrally dispersing the fluorescence from this slice over the other axis of our CCD camera.
 353 In such a measurement, the diffracted orders $\delta(|\mathbf{k}| - k_0 n_{\text{mode}}) \pm 2\pi/d(0, 1)$ appear as straight lines
 354 that intersect at $k_y = 0$ for the 2nd order Bragg diffraction conditions. In contrast, the diffracted
 355 orders $\delta(|\mathbf{k}| - k_0 n_{\text{WG}}) \pm 2\pi/d(1, 0)$ appear as the two parabola's, that have their minimum at the
 356 2nd order Bragg diffraction condition. If the dominant waveguide mode is TE (TM) polarized,
 357 i.e., tangential (radial) to the mode circles, this reasoning implies that the parabolic bands must be
 358 polarized along (crossed to) the slit, while the linear bands are polarized crossed to (resp. along)
 359 the slit. Measurements of the band structure with linear polarization analyzer along and across the

slit are shown in Fig. 4(g,h) The observed behavior clearly indicates that the features we observe are strongly TE polarized. Indeed, the TE mode has a strong electric field component in the plane of the particles, along their main polarizability tensor axes. The TM mode mainly provides field along the sample normal. Through the small in-plane field, however, coupling between TE and TM polarized slab modes is possible via scattering at the particles. Especially the fact that the upper parabola remains visible in Fig. 4(h) indicates TE-TM mixing.

VII. STOP GAP WIDTH

The measured band structures as function of particle size indicate a strong dependence of gap width on particle scattering strength, or detuning. To quantify this relation, we extract the relative stop gap width ($\Delta\omega/\omega$) and plot it versus particle size in Figure 5(a). A direct relation between stop gap width and a scattering parameter such as cross section is not unexpected. For instance, in 3D dielectric photonic crystals of spheres the relative stop gap width is given by⁴⁸

$$\frac{\Delta\omega}{\omega} = 4\pi \frac{\alpha}{V} \quad (7)$$

where α stands for (electrostatic) polarizability (real and positive for dielectric spheres), and V for the unit cell volume. At first sight it stands to reason that a similar relation holds in 2D plasmonic systems. However, in the plasmonic case the physics is richer, since α is a complex quantity, while stop gap widths must obviously be real and positive. There is no currently available theory that reports the equivalent of Eq. (7) for stop gap width in terms of scattering parameters of plasmon particles.

To bring out the dependence of stop gap width on scattering strength more clearly, we construct a "master diagram" that plots the data obtained here with the Rh6G-Rh700 FRET pair, and data obtained earlier with just Rh6G²⁰ as function of a normalized frequency detuning parameter. We use the detuning between particle plasmon and lasing wavelength $\omega_{\text{LSPR}} - \omega_{\text{lasing}}$, normalized to the bandwidth of the plasmon resonance (FWHM Γ_{LSPR}). Note that this is the only apparent relevant linewidth to normalize to in our system. The relevant single-particle frequency and linewidth are obtained by fitting a Lorentzian to the simulated particle response (specifically, $\sigma_{\text{scat}}\lambda^4 \propto |\alpha|^2$). The data in Fig. 4 taken with Rh700 as gain medium, appear at negative detuning, while data taken with Rh6G correspond to positive detuning. We remind the reader that for the Rh700 data we kept lasing frequency ω_{lasing} fixed (fixed pitch), while particle size tuned the plasmon resonance ω_{lasing}

388 onto the lasing condition. For positive detuning, data was taken with a fixed particle size of 110
389 nm, varying pitch from 360 to 400 nm.

The resulting stop gap width clearly drops when detuning in either direction away from zero detuning, however, in an asymmetric fashion. Stop gap widths are about three times higher for detuning to the blue of the resonance, then for equal detuning to the red of the resonance. Such an asymmetry could be expected, in the sense that even if one starts with a Lorentzian polarizability $\alpha(\omega)$ as in Eq. 1, the scattering response of a plasmon particle is asymmetric in frequency as a consequence of radiation damping (Eq. (2)). This is highlighted by plotting (cf. Fig. 5) the scattering cross section

$$\sigma_{\text{scatt}} = \frac{8\pi}{3} k^4 |\alpha|^2$$

390 for an archetypical Lorentzian scatterer alongside the data (taking typical Ohmic damping for sil-
391 ver ($\gamma = 0.05\omega_0$) and a particle volume chosen to obtain a scattering cross section at 80% of the
392 unitary limit ($3/2\pi\lambda^2$)). The stop gap width correlates well with the scattering cross section which
393 shows a similar asymmetry as the data. For reference, in blue the cross section from full-wave
394 simulations for each particle size (Fig. 1b), taken at the stop gap center frequency, is reproduced.
395 It should be noted that Fig. 5 reports no stop gap width for any sample at zero detuning, although
396 near-zero detuning is achieved for $2r > 100$ nm. As discussed below, for these large scatter-
397 ing strengths, the band structure we measure can not be trivially traced to the original four-band
398 crossing in a coupled-mode/slightly perturbed free-photon picture, hampering a stop gap width
399 assignment.

400 VIII. BAND STRUCTURE TOPOLOGY VERSUS DETUNING

401 We now turn to discussing more detailed features of the measured dispersion relations beyond
402 just stop gap width. Figure 6 shows three measured dispersion diagrams. Panel a, shows a disper-
403 sion diagram taken from Ref.²⁰, obtained on a sample that has the lasing condition well to the blue
404 of the localized surface plasmon resonance (Rh6G sample, $d = 380$ nm, 55 nm radius particle).
405 Panel c shows a dispersion diagram for the converse case, i.e., with the lasing condition well to
406 the red of the plasmon resonance (case (e), Fig. 4). The panel in the middle, finally, corresponds
407 to a case where the lasing condition is aligned to the plasmon resonance (Rh700 sample, particle
408 diameter 129 nm). These three detuning cases correspond to the separation into blue detuning,
409 zero detuning, and red detuning case that we also presented for our theory results in Fig. 2.

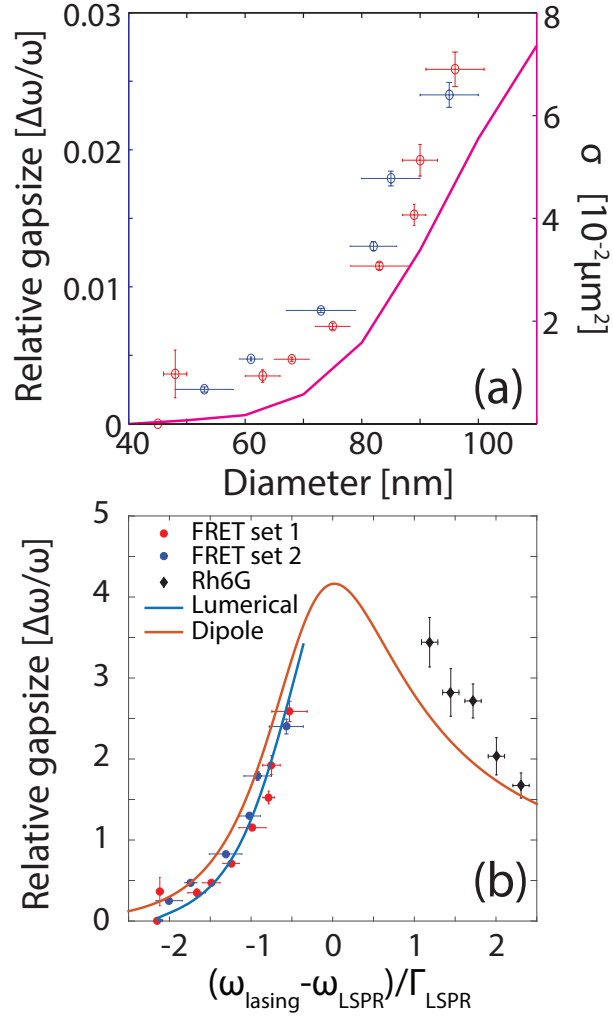


FIG. 5. (a) Relative stop gap width versus particle size. Red and blue points correspond to two distinct sample series. Error bars in particle size are from SEM measurements. The drawn line corresponds to the Lumerical-simulated extinction cross section. (b) Stop gap width versus normalized detuning between plasmon resonance and Bragg diffraction wavelength. Points in red and blue have been taken from Rh6G:Rh700 samples with large pitch (as in Fig. 4), while the black points at positive detuning are obtained using RH6G, with 110 nm particles and pitches from 360 to 400 nm²⁰. The red line represents the scattering cross section expected in a dipole model, while in blue the cross section versus diameter from Lumerical calculations is shown that is also plotted in (a).

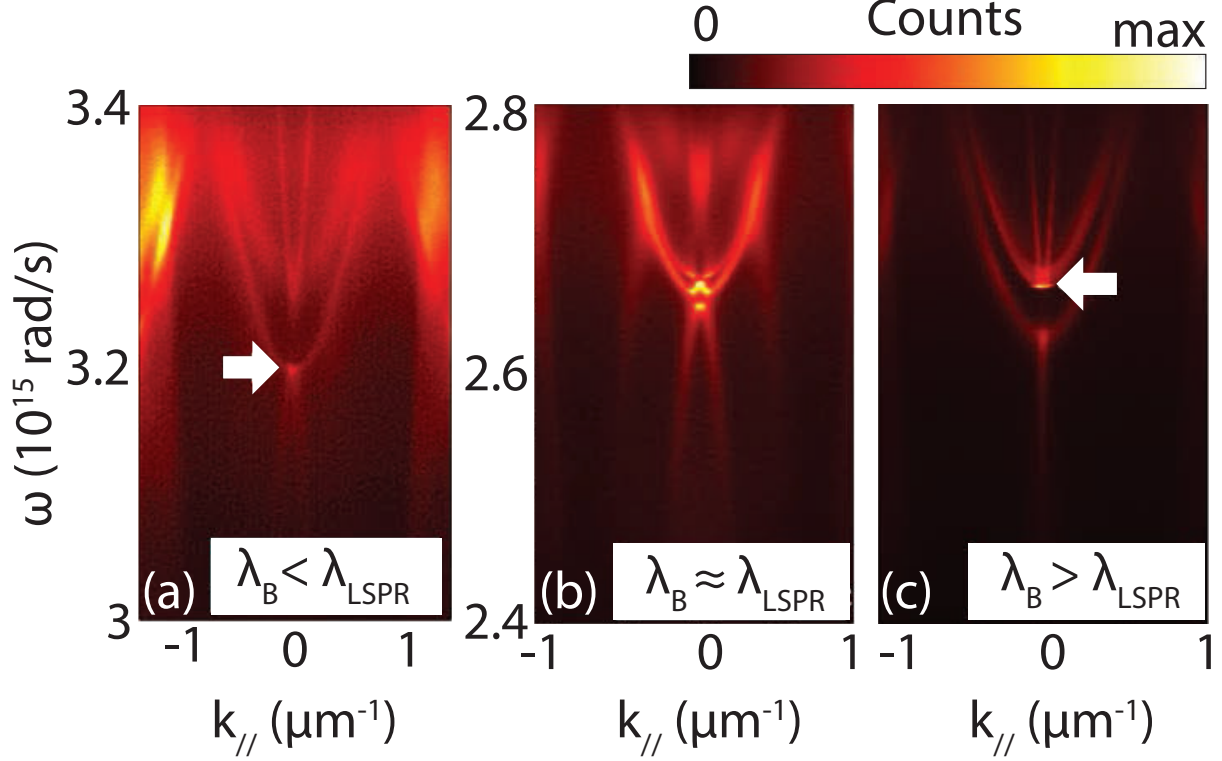


FIG. 6. Generic $\omega - k$ diagrams for three cases: lasing condition blue-detuned, red-detuned, and centered on the plasmon resonance (panels a, c and b). These concern $d = 380$, $2r = 55$ nm (panel (a)), $d = 460$, $2r = 129$ nm (b), and (c) $d = 460$, $2r = 86$ nm. For panel (a) we used Rh6G only, while the other panels used the Rh6G:Rh700 FRET mixture. White arrows indicate the $\omega - k$ -point on which the system lases first.

We note the following progression in the data. First, when the Bragg condition is well to the red of the localized surface plasmon resonance (negative detuning, panel c), the lower and upper parabola have their minima coincident with the maximum and minimum of the anticrossing linear dispersion relations, quite similar to nearly-free-photon band structure predictions would yield^{36,49}. Lasing in these samples always occurs on the upper band edge, consistent with the complex dispersion analysis in Figure 2. The fact that the parabola and the anticrossing lines share a common gap is consistent with the scalar coupled mode theory for dielectric DFB lasers (adapted to metal hole array plasmon lasers by van Exter et al.⁴⁹ (Fig. 4b)) in the limit that coupling by $\mathbf{G} = 2\pi/d(0, \pm 1)$ and $(\pm 1, 0)$ dominates, and $(\pm 1, \pm 1)$ scattering is weak. For the opposite-detuning case, i.e., panel (a) in which the Bragg condition occurs to the blue of the particle resonance (positive detuning), again two split parabola, and two anticrossing linear bands are retrieved, now with the upper parabola consistently very broad. For these samples lasing

occurs on the lower stop gap edge instead of the upper stop gap edge, again commensurate with the complex-valued dispersion analysis reported in Figure 2. Finally, when the particle plasmon and lasing condition coincide, i.e. panel b in Figure 6 the band structure is markedly different. The minimum of the lower parabola is pushed below the frequency range of the measurement, and a set of additional features has appeared that can not be trivially traced to the original four-band crossing in a coupled-mode/slightly perturbed free-photon picture (for which reason, the sample in panel b does not appear as a datapoint in Fig. 5). Lasing occurs on both apparent band edges, with similar thresholds.

IX. REAL SPACE COMSOL STUDY

Complementary to a wave vector space study that identifies which dispersion branches have low loss, yet good outcoupling, one can also perform a real space analysis that targets to understand what distinguishes the modes with large and low loss. A likely explanation carries over from coupled mode theory and the field of photonic crystals, where it is well known that gap edge modes are standing waves concentrated at different locations in the unit cell. For dielectric photonic crystals the band with most energy density in the dielectric (air) corresponds to the the lower (upper) band edge, giving rise to the terminology of "dielectric (air) band". One can hypothesize that also in plasmonic crystals one band will reside at, and one band will reside away from the plasmon particles. The energetic ordering, as well as the Ohmic loss, of these two bands could then be expected to flip when the sign of the scattering potential, i.e., polarizability α flips, which occurs as one goes from negative to positive detuning. In turn this would explain that opposite sign of detuning also implies a swap in the band edge that lases.

Since dipole models are not suited to obtain near fields, we consider a COMSOL 3D finite element simulation. As indices for the dielectric stack we take 1.46/1.65/1.0 - although the actual glass we use is not quartz but fused silica ($n=1.52$), and the SU8 index from ellipsometry is actually 1.60, not the datasheet value of 1.65. The reason for this choice is that it provides a larger separation between waveguide mode indices, and hence easier separation in the discussion, between waveguide modes, and plain diffraction into the glass. Fig. 7(a) shows calculated lattice extinction alongside the single particle resonance in panel (b). As particles we assume silver disks of height 30 nm and diameter 100 nm. The single-particle extinction (Fig. 7b) shows a strong resonance at $\omega = 2.76 \cdot 10^{15} \text{ s}^{-1}$, equivalent to 680 nm light, comparable to the result in Fig. 3. Next, we

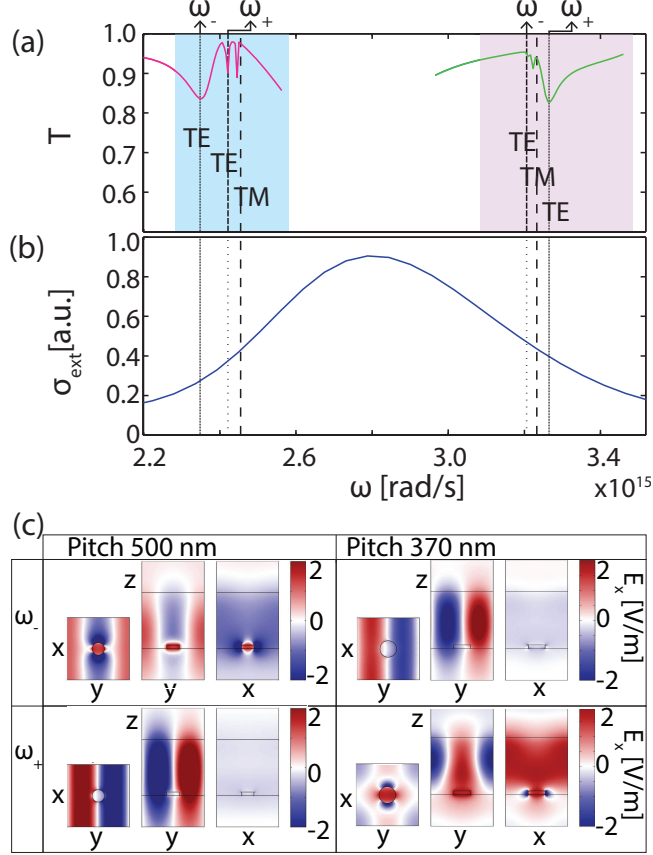


FIG. 7. The blue curve in the lower panel (b) shows the extinction cross section for a single silver disk with a height of 30 nm and a diameter of 100 nm on a substrate with index $n=1.46$, embedded in a waveguide with a refractive index of 1.65 and a thickness of 450 nm. Panel (a) shows transmission for an array of these particles with a pitch of 500 nm (pink) and 370 nm (green). The pink and blue areas represent the frequencies limited by $\omega = 2\pi c n_{\text{mat}} d$ with $n_{\text{mat}} = 1.65$ and 1.46 for both pitches, that would correspond to grazing angle grating coupling into solid SU8, or the glass. The dotted lines show the frequencies for which the waveguide mode without particles has a TE and a TM mode, as indicated. We label the broad and narrow dip that are associated to the stop gap edges as ω_- and ω_+ (near 2.4 resp. $3.25 \cdot 10^{15} \text{ s}^{-1}$ for pitches of 500 nm resp. 370). Panel (c): Crosscuts in the xy plane, xz and yz plane through one unit cell of in a particle array for frequencies ω_- and ω_+ indicated in panel (a), with m and 500 nm. Plotted is scattered field $E_x - E_{x,\text{in}}$ along the 1 V/m x -oriented incident field.

452 implemented Bloch-Floquet boundary conditions to obtain the diffractive properties upon plane
 453 wave driving incident from the glass side. We studied two pitches, i.e. 500 nm and 370 nm, to
 454 meet the 2nd order Bragg condition on either side of the resonance, and use slightly off-normal

excitation (0.5° along k_y) to make sure that symmetry does not forbid coupling.

Figure 7a shows the transmission in a small frequency range around the diffractive coupling condition for both pitches. The curves present the following three features. First, the generally high transmission is dominated by a relative broad (though still narrow compared to the plasmon resonance) asymmetric minimum that has the appearance of a Fano lineshape. Second, the spectra show two extremely narrow features. The frequency at which the two narrow features occur match very well with diffractive coupling to the TE and TM waveguide mode. We interpret the wide minimum, and the narrow TE feature as the relevant lower, and upper stop gap edge for the TE-like waveguide mode. This assignment is supported by examination of field cross cuts (see below). Note that for the large-pitch case $d = 500$ nm, the broad minimum occurs at a frequency *below* the narrow feature, while for the small-pitch case, the ordering is reversed. We examine the scattered fields (i.e., full field, minus the field that we calculate in absence of the particle) upon plane wave driving at the center frequencies of the broad and narrow minima. Figure 7c shows the scattered field component E_x that is along the incident polarization for both pitches, and for each pitch at the labelled lower and upper gap edge ω_{\pm} . The vertical cuts show that the transverse field distributions is essentially the mode profile of a TE mode. At the frequency of the narrow feature (ω_+ resp. ω_- for the large resp small pitch case), the scattered field has a nodal plane at the particle, and resides mainly away from it. Conversely, at the broad minimum in transmission, the associated field plot shows strong excitation of the particle. The COMSOL simulation hence corroborates the interpretation that lasing selects the stop gap edge that corresponds to the Bloch mode that forms a standing wave with energy density predominantly away from the particle, as this is the lowest-loss mode that still couples out. As one goes through resonance, the stop gap edge to which this standing wave corresponds is reversed, as the real part of the polarizability flips sign.

X. CONCLUSIONS AND OUTLOOK

In summary, we have shown how the optical response of plasmonic scatterers affects the band diagram of a plasmon particle array embedded in a dye doped waveguide layer. By combining data for lasers with various particle sizes, pitches, and two gain media near 590 nm and FRET-based gain at 700 nm, we were able to systematically map the behavior of plasmon lattice lasers as function of the detuning between particle resonance and lasing condition as set by the lattice periodicity. A main conclusion is that the stop gap width in the band structure of the plasmon lattice

lasers is much larger than in dielectric distributed feedback lasers, and is essentially proportional to the particle scattering cross section. Commensurate with the complex lattice dispersion that we calculate from an electrodynamic coupled dipole model, the stop gap edge that gives rise to lasing is always the one closest to the particle resonance, and corresponds to the condition of a low loss Bloch mode that at the same time has nonzero outcoupling efficiency. While the strong scattering by plasmon particles couples TE and TM mode, the outcoupled light is of TE nature. When plasmon and lattice resonance are aligned, the band structure is particularly far from a nearly-free photon approximation, which is qualitatively correct only for lasing far to the red of the plasmon resonance.

We note that our work also provides pointers for further experiments and theory. Any theory must account at least for the scaling of stop gap with scattering strength, the qualitatively very different band structure at zero detuning, and for subtle features such as where the mode resides and what mode has least loss, depending on the choice of detuning. It is a surprisingly challenging problem to build a theory for this system. Coupled mode theory^{36,49} would treat the particles as a weak perturbation, and is essentially valid only for small dielectric perturbations. Numerically the difficulties in extending it to plasmon particles are clear from the fact that Fourier modal, i.e., plane wave expansion, methods are very poorly convergent for plasmon particle gratings.²⁰ Coupled dipole theory as presented here can treat complex-valued dispersion relations at very large scattering strength, yet only provides partial insight in the laser physics. A more refined treatment of near fields and of nonlinear dynamics of lasing above threshold is required to quantitatively account for loss, local pump and Purcell enhancements, the overlap of modes with the gain medium and gain dynamics. Finite element treatment, finally is accurate for near field, can include gain²⁹ and allows complicated unit cell geometries. However, although possible, this approach may be significantly more computationally demanding when extended to deal with *complex-valued* dispersion relations of decaying modes. Experiments that could guide these theoretical efforts would for instance include studying variations in particle material, or using core-shell geometries, to independently vary physical particle volume, loss and scattering cross sections. Also we envision that using gain media of different spatial distributions, be it arranged lithographically or by controlling the optical pump field⁵⁰, and gain media of different quantum efficiency, will allow to unravel the role of near field enhancements. Finally we note that our considerations likely also carry over to lasing structures that use surface lattice resonances, but no waveguide^{17–19}. In case of surface lattice resonances there is no waveguide, but lasing does occur at resonance crossings^{17–19}.

517 According to Rodriguez et al. 51, extinction spectra of such systems also can show gaps, with a
 518 width that depends on the tuning of local plasmon resonance and diffraction condition. In our
 519 system, evidently lasing occurs on a hybrid plasmonic-photonic mode where the waveguide helps
 520 to optimize mode overlap with the scatterers, thereby aiding the opening of a stop gap that is wide.

521 ACKNOWLEDGMENTS

522 We thank Marko Kamp for technical support with the experiment, and Alexei Halpin for a crit-
 523 ical reading of the manuscript. This work is part of the research program of the Foundation for
 524 Fundamental Research on Matter (FOM), which was financially supported by The Netherlands Or-
 525 ganization for Scientific Research (NWO). This work was furthermore supported by NanoNextNL,
 526 a microtechnology and nanotechnology consortium of the Government of the Netherlands and 130
 527 partners. AA was partially supported by a Visiting Professorship of the KNAW, the Royal Nether-
 528 lands Academy of Arts and Sciences. YH and AA were also supported by the Air Force Office of
 529 Scientific Research, the Welch Foundation with grant No. F-1802, and the Simons Foundation.

530 Appendix A: 1D Green's function

First we define normalized longitudinal wavenumbers $\zeta_i^X = \sqrt{\epsilon_{ri} - \xi_X^2}$, with $X = TE/TM$ and subject to the radiation condition $\text{Im}\{\zeta_i^X\} \geq 0$. Then, the 1D Green's function used in Eq.(5) is given by

$$g(\omega, z, z') = \frac{1}{2} \frac{Z_2^X}{D_X} \left(e^{ik_z^X |z-z'|} + R_1^X e^{ik_z^X (2h-(z+z'))} \right. \\ \left. + R_3^X e^{ik_z^X (z+z')} + R_1^X R_3^X e^{ik_z^X (2h-|z-z'|)} \right) \quad (\text{A1})$$

531 where h is the SU8 layer thickness and $k_z^X = k_0 \zeta_2^X$, and

$$R_i^X = \frac{Z_i^X - Z_2^X}{Z_i^X + Z_2^X}, \quad i = 1, 3$$

532

$$Z_i^{TM} = \eta_0 \frac{\zeta_1^{TM}}{\epsilon_{ri}}, \quad Z_i^{TE} = \frac{\eta_0}{\zeta_i^{TE}} \quad i = 1, 2, 3,$$

533 and

$$D_X = \frac{d}{d\xi} (1 - R_1^X R_3^X e^{2ik_0 \zeta_2^X h}) \Big|_{\xi_X = k_X/k_0}.$$

534 Appendix B: Ewald summation

The convergence of the infinite summation in Eq. (3) can be significantly accelerated by using the Ewald summation technique^{31–33,37–42}. First, we write

$$C(\omega, k_x, k_y) = 2A_{TE} \left(S(k_{TE}) + \frac{S_{xx}(k_{TE})}{k_{TE}^2} \right) - 2A_{TM} \frac{S_{xx}(k_{TM})}{k_{TM}^2} \quad (\text{B1})$$

535 with $k_{TE} = k_0 \xi_{TE}$, and $k_{TM} = k_0 \xi_{TM}$, and

$$S(k) = \lim_{x'y' \rightarrow 0} \sum' H_0^{(1)}(kR_{mn}) e^{id(mk_x + nk_y)}, \quad (\text{B2a})$$

536

$$S_{xx}(k) = \partial_{x'x'} S(k) \quad (\text{B2b})$$

537 where $R_{mn} = \sqrt{(x' - md)^2 + (y' - nd)^2}$. The primed summation sign in Eq.(B2a) is used to
538 exclude the $(m, n) = (0, 0)$ term from the infinite two dimensional summation. The summation
539 can also be written as

$$S(k) = \lim_{x'y' \rightarrow 0} \sum H_0^{(1)}(kR_{mn}) e^{id(mk_x + nk_y)} - H_0^{(1)}(k\rho'),$$

540 where $\rho' = \sqrt{x'^2 + y'^2}$. The unprimed summation is used for infinite summation $(m, n) \in$
541 $(-\infty, \infty) \times (-\infty, \infty)$. Next we replace the Hankel function by one of its integral representa-
542 tions

$$H_0^{(1)}(kR_{mn}) = -\frac{2i}{\pi} \int_0^\infty \frac{du}{u} e^{(k^2/4u^2 - R_{mn}^2 u^2)}.$$

543 Note that since $R_{mn}^2 > 0$, and assuming that $k^2 > 0$, to formally guarantee convergence of the inte-
544 gral representation in Eq.(B3) we have to require that u pass to infinity along the line $\arg u = -\pi/4$.
545 However, once we use this representation and derive an alternative, rapidly converging representa-
546 tion for the summation, we may apply Cauchy theorem and calculate the required integrals along
547 a more convenient path.

548 The semi-infinite integration path above is decomposed into two intervals, $0 \rightarrow E$, and $E \rightarrow$
549 ∞ , where E is an arbitrarily chosen constant picked as a trade off between fast convergence of S_1
550 and S_2 . We define

$$S_1 = \sum -\frac{2i}{\pi} \int_0^E \frac{du}{u} e^{(k^2/4u^2 - R_{mn}^2 u^2)} e^{id(mk_x + nk_y)} \quad (\text{B3a})$$

551

$$S_2 = \sum' -\frac{2i}{\pi} \int_E^\infty \frac{du}{u} e^{(k^2/4u^2 - R_{mn}^2 u^2)} e^{id(mk_x + nk_y)} \quad (\text{B3b})$$

552

$$C = \frac{2i}{\pi} \int_0^E \frac{du}{u} e^{(k^2/4u^2 - \rho'^2 u^2)} \quad (\text{B3c})$$

553 such that $S = S_1 + S_2 + C$. Note that as long as $E \gg k/2$, the integration in the summands
 554 of S_2 yields a Gaussian decay of the summands with respect to the summation indexes hence the
 555 summation over this part of the integral convergence rapidly. Similarly, the integration required to
 556 calculate C converge rapidly. The only issue left is the slow convergence of S_1 which is similar
 557 to the poor convergence of the original series. In this case, however, we are able to apply Poisson
 558 summation to accelerate the convergence. We obtain,

$$S_1 = \frac{4i}{d^2} \sum_{p,q} \frac{e^{k_{zpq}^2/4E^2}}{k_{zpq}^2} \quad (\text{B4})$$

559 where $\mathbf{k}_{ppq} = (k_x, k_y) - 2\pi/d(p, q)$, and $k_{zpq}^2 = k^2 - \mathbf{k}_{ppq} \cdot \mathbf{k}_{ppq}$, $p, q \in \mathcal{Z}^2$ (\mathcal{Z} denotes the
 560 set of integers). The convergence of the summation for S_1 in its new representation is Gaussian,
 561 therefore, practically only a few terms are required. Finally, we have $S_{xx} = S_{1xx} + S_{2xx} + C_{xx}$
 562 where

$$S_{1xx} = -\frac{4i}{d^2} \sum_{p,q} \frac{e^{k_{zpq}^2/4E^2}}{k_{zpq}^2} \left(k_x - \frac{2\pi}{d}p\right)^2 \quad (\text{B5a})$$

$$S_{2xx} = \sum' \frac{4i}{\pi} \int_E^\infty du (1 - 2m^2 d^2 u^2) u \quad (\text{B5b})$$

$$\times e^{(k^2/4u^2 - R_{mn}^2 u^2)} e^{id(mk_x + nk_y)}$$

563

$$C_{xx} = -\frac{4i}{\pi} \int_0^E du u e^{(k^2/4u^2 - \rho'^2 u^2)} \quad (\text{B5c})$$

564 ¹ I. D. W. Samuel and G. A. Turnbull, Chem. Rev. **107**, 1272 (2007).

565 ² G. Heliotis, R. D. Xia, G. A. Turnbull, P. Andrew, W. L. Barnes, I. D. W. Samuel, and D. D. C. Bradley,
 566 Adv. Funct. Mater. **14**, 91 (2004).

567 ³ G. A. Turnbull, P. Andrew, M. Jory, W. Barnes, and I. Samuel, Phys. Rev. B **64**, 125122 (2001).

568 ⁴ P. Del Carro, A. Camposeo, R. Stabile, E. Mele, L. Persano, R. Cingolani, and D. Pisignano, Appl.
 569 Phys. Lett. **89**, 201105 (2006).

570 ⁵ E. Mele, A. Camposeo, R. Stabile, P. Del Carro, F. Di Benedetto, L. Persano, R. Cingolani, and D. Pisig-
 571 nano, Appl. Phys. Lett **89**, 131109 (2006).

- 572 ⁶ S. A. Maier, *Plasmonics: Fundamentals and Applications* (Springer, 2007).
- 573 ⁷ G. M. Akselrod, C. Argyropoulos, T. B. Hoang, C. Cirac, C. Fang, J. Huang, D. R. Smith, and M. H.
574 Mikkelsen, *Nat. Photonics* **8**, 835 (2014).
- 575 ⁸ C. Belacel, B. Habert, F. Bigourdan, F. Marquier, J.-P. Hugonin, S. Michaelis de Vasconcellos,
576 X. Lafosse, L. Coolen, C. Schwob, C. Javaux, B. Dubertret, J.-J. Greffet, P. Senellart, and A. Maitre,
577 *Nano Lett.* **13**, 1516 (2013).
- 578 ⁹ E. J. R. Vesseur, F. Javier Garcia de Abajo, and A. Polman, *Phys. Rev. B* **82**, 165419 (2010).
- 579 ¹⁰ S. Murai, M. A. Verschuuren, G. Lozano, G. Pirruccio, S. R. K. Rodriguez, and J. G. Rivas, *Opt. Express*
580 **21**, 4250 (2013).
- 581 ¹¹ G. Vecchi, V. Giannini, and J. Gómez Rivas, *Phys. Rev. Lett.* **102**, 146807 (2009).
- 582 ¹² A. G. Nikitin, A. V. Kabashin, and H. Dallaporta, *Opt. Express* **20**, 27941 (2012).
- 583 ¹³ P. L. Stiles, J. A. Dieringer, N. C. Shah, and R. R. Van Duyne, *Annu. Rev. Anal. Chem.* **1**, 601 (2008).
- 584 ¹⁴ M. E. Stewart, C. R. Anderton, L. B. Thompson, J. Maria, S. K. Gray, J. A. Rogers, and R. G. Nuzzo,
585 *Chem. Rev.* **108**, 494 (2008).
- 586 ¹⁵ J. N. Anker, W. P. Hall, O. Lyandres, N. C. Shah, J. Zhao, and R. P. Van Duyne, *Nat. Mater.* **7**, 442
587 (2008).
- 588 ¹⁶ G. Lozano, D. J. Louwers, S. R. K. Rodriguez, S. Murai, O. T. A. Jansen, M. A. Verschuuren, and J. G.
589 Rivas, *Light. Sci. Appl.* **2**, e66 (2013).
- 590 ¹⁷ W. Zhou, M. Dridi, J. Y. Suh, C. H. Kim, D. T. Co, M. R. Wasielewski, G. C. Schatz, and T. W. Odom,
591 *Nat. Nanotechnol.* **8**, 506 (2013).
- 592 ¹⁸ J. Y. Suh, C. H. Kim, W. Zhou, M. D. Huntington, D. T. Co, M. R. Wasielewski, and T. W. Odom, *Nano*
593 *Letters* **12**, 5769 (2012).
- 594 ¹⁹ A. Yang, T. B. Hoang, M. Dridi, C. Deeb, M. H. Mikkelsen, G. C. Schatz, and T. W. Odom, *Nat.*
595 *Commun.* **6**, 6939 (2015).
- 596 ²⁰ A. H. Schokker and A. F. Koenderink, *Phys. Rev. B* **90**, 155452 (2014).
- 597 ²¹ A. H. Schokker and A. F. Koenderink, *ACS Photonics* **2**, 1289 (2015).
- 598 ²² H. P. Urbach and G. L. J. A. Rikken, *Phys. Rev. A* **57**, 3913 (1997).
- 599 ²³ M. J. Weber, *Handbook of Optical Constants of Materials* (CRC Press, 2003).
- 600 ²⁴ L. Zhao, K. L. Kelly, and G. C. Schatz, *J. Phys. Chem. B* **107**, 7343 (2003).
- 601 ²⁵ A. Bouhelier, R. Bachelot, J. Im, G. Wiederrecht, G. Lerondel, S. Kostcheev, and P. Royer, *J. Phys.*
602 *Chem. B* **109**, 3195 (2005).

²⁶ M. Meier and A. Wokaun, Opt. Lett. **8**, 581 (1983).
²⁷ M. Dridi and G. C. Schatz, J. Opt. Soc. Am. B **30**, 2791 (2013).
²⁸ J.-P. Martikainen, T. K. Hakala, H. T. Rekola, and P. Törmä, J. Opt. **18**, 024006 (2016).
²⁹ J. Cuerda, F. Rüting, F. J. García-Vidal, and J. Bravo-Abad, Phys. Rev. B **91**, 041118 (2015).
³⁰ P. de Vries, D. V. van Coevorden, and A. Lagendijk, Rev. Mod. Phys. **70**, 447 (1998).
³¹ F. Capolino, D. R. Jackson, D. R. Wilton, and L. B. Felsen, IEEE Trans. Antennas Propag. **55**, 1644 (2007).
³² F. J. G. de Abajo, Rev. Mod. Phys. **79**, 1267 (2007).
³³ A. Kwadrin and A. F. Koenderink, Phys. Rev. B **89**, 045120 (2014).
³⁴ Y. Hadad and B. Z. Steinberg, 2010 URSI International Symposium on Electromagnetic Theory , 680 (2010).
³⁵ D. Van Orden, Y. Fainman, and V. Lomakin, Opt. Lett. **34**, 422 (2010).
³⁶ H. Kogelnik and C. Shank, Appl. Phys. Lett. **18**, 152 (1971).
³⁷ S. Steshenko, F. Capolino, P. Alitalo, and S. Tretyakov, Phys. Rev. E **84**, 016607 (2011).
³⁸ P. Lunnemann, I. Sersic, and A. F. Koenderink, Phys. Rev. B **88**, 245109 (2013).
³⁹ A. L. Fructos, S. Campione, F. Capolino, and F. Mesa, J. Opt. Soc. Am. B **28**, 1446 (2011).
⁴⁰ K. Kambe, Z. Naturforsch. **23a**, 1280 (1968).
⁴¹ C. M. Linton, SIAM Rev. **52**, 630 (2010).
⁴² Y. Mazar and B. Z. Steinberg, Phys. Rev. Lett. **112**, 153901 (2014).
⁴³ M. Agio and A. Alù, *Optical Antennas*, p31 (Cambridge University Press, 2013).
⁴⁴ A. Mohtashami and A. F. Koenderink, New Journal of Physics **15**, 043017 (2013).
⁴⁵ J. R. Lakowicz, *Principles of Fluorescence Spectroscopy* (Springer, 2006).
⁴⁶ K. B. Eisenthal and S. Siegel, J. Chem. Phys. **41**, 652 (1964).
⁴⁷ T. Förster, Annalen der Physik **437**, 55 (1948).
⁴⁸ W. L. Vos, R. Sprik, A. van Blaaderen, A. Imhof, A. Lagendijk, and G. Wegdam, Phys. Rev. B **55**, 1903 (1997).
⁴⁹ M. P. van Exter, V. T. Tenner, F. van Beijnum, M. J. A. de Dood, P. J. van Veldhoven, E. J. Geluk, and G. W. 't Hooft, Opt. Express **21**, 27422 (2013).
⁵⁰ G. Pirruccio, M. Ramezani, S. R.-K. Rodriguez, and J. G. Rivas, Phys. Rev. Lett. **116**, 103002 (2016).
⁵¹ S. R. K. Rodriguez, A. Abass, B. Maes, O. T. A. Janssen, G. Vecchi, and J. Gómez Rivas, Phys. Rev. X **1**, 021019 (2011).